JOURNAL OF PROPULSION AND POWER
Vol. 24, No. 2, March–April 2008

Boundary-Layer Effects on Internal Flow Choking in Dual-Thrust Solid Rocket Motors

V. R. Sanal Kumar*
Vikram Sarabhai Space Centre, Trivandrum 695 022, Kerala, India
B. N. Raghunandan†
Indian Institute of Science, Bangalore 560 012, India
T. Kawakami‡
Hosei University, Tokyo 184-8584, Japan
H. D. Kim§
Andong National University, Andong 760-749, Republic of Korea
T. Setoguchi§
Saga University, Saga 840-8502, Japan
and
S. Raghunathan¶
Queen's University of Belfast, Northern Ireland BT7 1NN, United Kingdom

DOI: 10.2514/1.30649

Theoretical studies have been carried out to examine internal flow choking in the inert simulators of a dual-thrust motor. Using a two-dimensional *k*–omega turbulence model, detailed parametric studies have been carried out to examine aerodynamic choking and the existence of a *fluid throat* at the transition region during the startup transient of dual-thrust motors. This code solves standard *k*–omega turbulence equations with shear flow corrections using a coupled second-order-implicit unsteady formulation. In the numerical study, a fully implicit finite volume scheme of the compressible, Reynolds-averaged, Navier–Stokes equations is employed. It was observed that, at the subsonic inflow conditions, there is a possibility of the occurrence of internal flow choking in dual-thrust motors due to the formation of a *fluid throat* at the beginning of the transition region induced by area blockage caused by boundary-layer-displacement thickness. It has been observed that a 55% increase in the upstream port area of the dual-thrust motor contributes to a 25% reduction in blockage factor at the transition region, which could negate the internal flow choking and supplement with an early choking of the dual-thrust motor nozzle. If the height of the upstream port relative to the motor length is too small, the developing boundary layers from either side of the port can interact, leading to a choked flow. On the other hand, if the developing boundary layers are far enough apart, then choking does not occur. The blockage factor is greater in magnitude for the choked case than for the unchoked case. More tangible explanations are presented in this paper for the boundary-layer blockage and the internal flow choking in dual-thrust motors, which hitherto has been unexplored.

Nomenclature

a = local speed of sound
d = upstream port diameter of the dual-thrust motor
L = length of the dual-thrust motor
M = Mach number
M_w = molecular weight
P_{op} = operating pressure
p = pressure
Q = volumetric flow rate
R = gas constant
Re = Reynolds number
T = temperature
t = time
U = mean flow velocity at a cross section
$U_{\max}$ = maximum axial velocity at a cross section
U_o = initial inlet velocity
u = velocity magnitude
x = coordinate in the axial direction
y = Cartesian coordinate
γ = ratio of specific heat
δ^* = displacement thickness
ε = turbulent dissipation rate
μ = dynamic viscosity
μ_t = turbulent viscosity
ρ = density
σ = turbulent Prandtl number
Ω = angular velocity
ω = specific dissipation rate

Presented as Paper 4432 at the 42nd AIAA Joint Propulsion Conference, California, USA, 10–12 July 2006; received 24 February 2007; revision received 16 August 2007; accepted for publication 31 August 2007.

*Scientific Ambassador and Scientist/Engineer, Propulsion Group; also Professor and Head, Department of Aeronautical Engineering, M. V. Jayaraman College of Engineering, Bangalore 560 067, India; rsanal@hotmail.com, sanal@aero.iisc.ernet.in.
†Professor and Chairman, Department of Aerospace Engineering.
‡Professor and Head, Department of Mechanical Engineering, College of Engineering.
§Professor of Mechanical Engineering.
¶Professor of Aeronautical Engineering, Bombardier Aerospace—Royal Academy Chair. Associate Fellow AIAA.

Introduction

A DETAILED picture of the internal flow during the starting transient of solid rocket motors (SRMs) is of interest for several reasons, in addition to the motor performance itself [1,2]. Starting transient is defined in this paper as the time interval between the

application of the ignition signal and the instant at which the motor attains its equilibrium or designed operating conditions. Although a great deal of research has been done in the area of solid rockets for more than six decades, the accurate prediction and reduction of an unusual pressure spike and pressure-rise rate often observed during the starting transient of high-velocity transient motors with narrow ports and steep divergence/protrusions in the grain have remained intangible problems. This is particularly true in the case of dual-thrust motors (DTMs) [2–11]. Two distinguishing features of DTMs are their high-volume loading and the unusual port configuration necessitated by the dual-thrust needs.

Ikawa and Laspesa [12] reported that, during the first launching of the space shuttle from the eastern test range, the launch vehicle experienced the propagations of a strongly impulsive compression wave. This wave was induced by the SRM ignition and was emanating from the large SRM duct openings. The analysis further showed that the compression wave created by ignition of the main grain was the cause of the ignition overpressure on the launch pad [13]. Alestra et al. [14] reported that the ARIENE 5 launcher experienced an overpressure load during the liftoff phase. The overpressure is composed of the ignition overpressure, which emanates from the launch pad, and the duct overpressure, which emanates from the launch ducts. It was reported that, in the Indian industry, a certain class of SRMs with divergent ports experienced ignition overpressure and a pressure-rise rate (see Figs. 1 and 2)[2–11].

In the literature, many remedies have been suggested to eliminate the unacceptable ignition pressure spike with reference to erosive

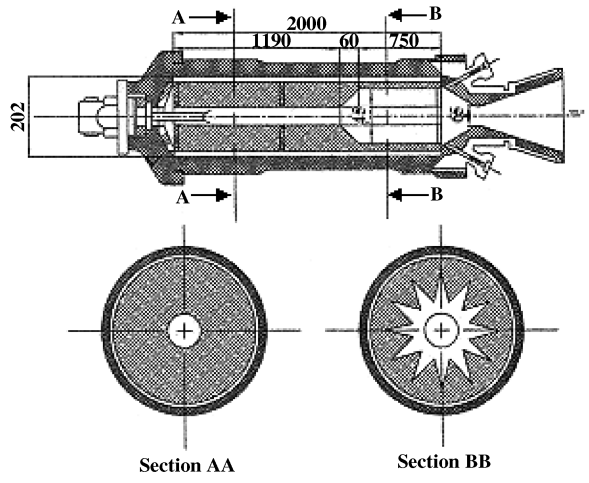

a)

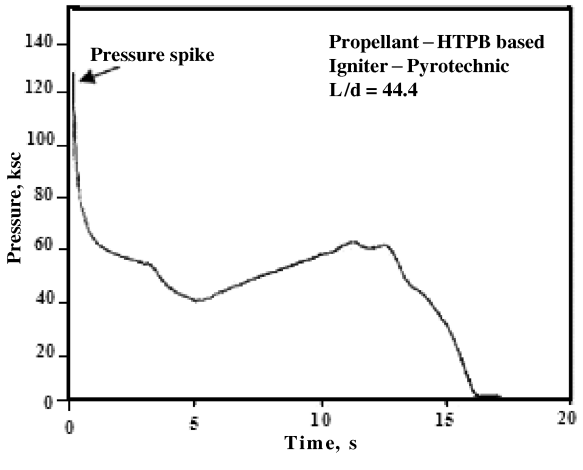

b)

Fig. 1 Pressure-time curve of a dual-thrust motor showing the unusual ignition spike during the full motor static test (corresponding motor configuration is shown in Fig. 1a).

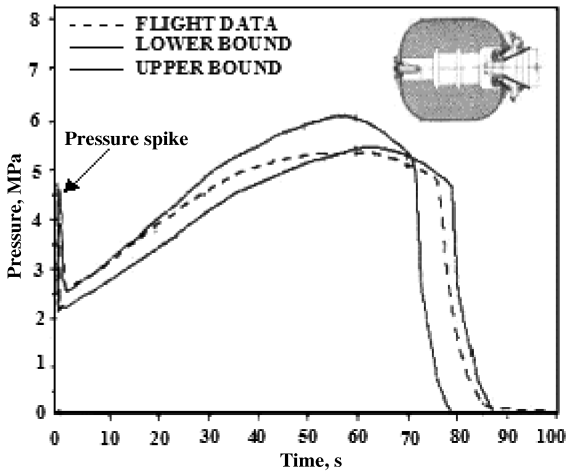

Fig. 2 Pressure-time history of an upper stage flight motor showing the ignition spike as 1.8 times the equilibrium pressure (configuration is shown in inset)[11]. Upper and lower bounds are selected based on full motor static test experience.

burning, transient/dynamic burning, propellant surface (as-cast/machined) preheating effect, radiation, flame spread dynamics, acoustic oscillations, grain deformation, ignition delay, propellant properties, nozzle closure burst pressure effects, thermal choking, choking due to oversized igniter, composition of igniter products, igniter size, its location and ballistics, etc [1,9–16]. Despite the fact that many of these techniques could reduce the ignition pressure spike and pressure-rise rate of a certain class of SRMs with divergent ports, none of these attempts could negate the unusual ignition pressure spike observed in the DTM [2–4]. Nevertheless, through empirical techniques, increasing the upstream port area of the motor has often been proposed as one of the remedies for eliminating the unusual ignition pressure spike of the DTM. Unfortunately, this reduces the propellant loading density and affects the high-performance nature of the rocket motor due to the envelop restriction. Hence, the elimination of the unusual ignition pressure spike and the pressure-rise rate without sacrificing the basic grain configuration or the volume loading became a meaningful and a challenging design objective for further studies [2–11].

Although many studies have been reported on ignition transient and on shock-boundary-layer interaction, none of these studies focused on the joint effect of the igniter jet, the grain geometry-dependent driving forces, and the boundary-layer effects on the formation of shock waves during the starting transient of solid rocket motors with divergent ports [15–36]. Of late, Sanal Kumar et al. [2–4] reported the formation of shock waves in DTMs during the ignition transient phase with different physical origins, which has received considerable attention in the scientific community. The motivation for the present study emanates from the desire to explain the phenomena or mechanism(s) responsible for the internal flow choking in a certain class of dual-thrust motors with a narrow-upstream port and steep divergence in the grain. This comprehensive paper is a continuation and also a consolidation of the previous companion AIAA Notes for establishing the intrinsic flow physics pertinent to internal flow choking in dual-thrust motors [2–4]. The implication of the internal flow choking can be quite serious for a dual-thrust motor. The internal flow choking results in the formation of shock waves inside the rocket motor. The shock waves and the new turbulence level will alter the location of the reattachment/secondary ignition point and also enhance the heat flux to the propellant surface, which will lead to an undesirable startup transient. In this paper, inert (unignited) simulators of dual-thrust motors are deliberately selected for parametric analytical studies to examine the various fundamental fluid-dynamics processes pertinent to the internal flow choking during the starting transient, without complications arising from the propellant combustion.

This paper addresses the design challenges associated with the development of high-performance dual-thrust motors because of

their large size, high length-to-diameter ratio, and demanding thrust-time trace shape requirements. The model reliability is further improved by using extensive experimental data. In addition to this modeling approach, the development of likelihood plans covers the remaining prediction uncertainties and readily allows fine tuning of the propellant grain configuration to meet the design objectives before the first static test of a new generation motors. This approach promises to produce an optimum and also profitable flight motor grain design that meets all performance objectives while accommodating program development uncertainties.

Numerical Methodology

Numerical simulations have been carried out with the help of a two-dimensional standard *k*–omega model. This turbulence model is an empirical model based on model transport equations for the turbulence kinetic energy and a specific dissipation rate [37]. This code solves standard *k*–omega turbulence equations with shear flow corrections using a coupled second-order-implicit unsteady formulation. In the numerical study, a fully implicit finite volume scheme of the compressible, Reynolds-averaged, Navier–Stokes equations is employed. Compared to other available models, this model could well predict the turbulence transition in duct flows and has been validated through benchmark solutions. Moreover the previous experimental results of Krall and Sparrow [17] and Stevens and Fry [18] supported our model selection for this specific study. Therefore, this model has been used for demonstrating the flow physics involved during the internal flow choking of inert simulators of DTM.

Compressible Flow Model

Compressibility effects are encountered in gas flows at high velocity and/or in which there are large pressure variations. When the flow velocity approaches or exceeds the speed of sound or when the pressure change in the system is large, the variation of the gas density with pressure has a significant impact on the flow velocity, pressure, and temperature. Compressible flows create a unique set of flow physics for which one must be aware of the special input requirements and appropriate solution techniques. Compressible flows can be characterized by the value of the Mach number. As the Mach number approaches 1.0, compressibility effects become important. When the Mach number exceeds 1.0, the flow is termed supersonic and may contain shocks and expansion that can impact the flow pattern significantly. Compressible flows are typically characterized by the total pressure P_0 and total temperature T_0 of the flow. The following relationships describe the variation of the static pressure and temperature in this flow model as the velocity/Mach number changes under isentropic conditions:

$$\frac{P_0}{p} = \left(1 + \frac{\gamma - 1}{2} M^2\right)^{\gamma/\gamma - 1} \tag{1}$$

$$\frac{T_0}{T} = 1 + \frac{\gamma - 1}{2} M^2 \tag{2}$$

Equation (1) predicts a choked flow ($M = 1.0$) at an isentropic pressure ratio. Note that in this model the choked flow condition will be established at the point of minimum flow area. In the subsequent area expansion, the flow may either accelerate to a supersonic flow in which the pressure will continue to drop or return to subsonic flow conditions, decelerating with a pressure rise. If a supersonic flow is exposed to an imposed pressure increase, a shock will occur, with a sudden pressure rise and deceleration accomplished across the shock.

In this model, the compressible flows are described by the standard continuity and momentum equations with the inclusion of the compressible treatment of the density, which is given next.

For compressible flows, the ideal gas law is written in the following form:

$$\rho = \frac{p_{\text{op}} + p}{\frac{R}{M_w} T} \tag{3}$$

The temperature, T, can be computed from the energy equation. The energy equation solved by the code will incorporate the coupling between the flow velocity and the static temperature.

The viscosity is determined from the Sutherland formula, given by

$$\mu = \frac{(1 + S)T^{3/2}}{T + S} \tag{4}$$

where $S = 110.4/288.15$.

Standard *k–ω* Model

This model is an empirical model based on model transport equations for the turbulence kinetic energy (k) and a specific dissipation rate (ω). This code solves standard *k*–omega turbulence equations with shear flow corrections using a coupled second-order-implicit unsteady formulation. The turbulence kinetic energy and specific dissipation rate are obtained from the following two transport equations:

$$\frac{\partial}{\partial t}(\rho k) + \frac{\partial}{\partial x_i}(\rho k u_i) = \frac{\partial}{\partial x_j}\left(\Gamma_k \frac{\partial k}{\partial x_j}\right) + G_k - Y_k + S_k \tag{5}$$

$$\frac{\partial}{\partial t}(\rho \omega) + \frac{\partial}{\partial x_i}(\rho \omega u_i) = \frac{\partial}{\partial x_j}\left(\Gamma_\omega \frac{\partial \omega}{\partial x_j}\right) + G_\omega - Y_\omega + S_\omega \tag{6}$$

In these equations, G_k represents the generation of turbulent kinetic energy due to the mean velocity gradient. G_ω represents the generation of ω. Γ_k and Γ_ω represent the effective diffusivity of k and ω, respectively. Y_k and Y_k represent the dissipation of k and ω due to turbulence. S_k and S_ω are user-defined functions.

$$\Gamma_k = \mu + \frac{\mu_t}{\sigma_k} \tag{7}$$

$$\Gamma_\omega = \mu + \frac{\mu_t}{\sigma_\omega} \tag{8}$$

$$\mu_t = \alpha^* \frac{\rho k}{\omega} \tag{9}$$

The coefficient α^* damps the turbulent viscosity, causing a low Reynolds number correction, which is given as

$$\alpha^* = \alpha^*_\infty(\alpha^*_o + 0.167 Re_t)/(1 + 0.167 Re_t) \tag{10}$$

where $Re_t = \rho k/\mu\omega$, $\alpha^*_o = 0.024$

$$G_k = -\overline{\rho u_i' u_j'} \frac{\partial u_j}{\partial x_i} \tag{11}$$

$$G_\omega = \alpha \frac{\omega}{k} G_k \tag{12}$$

$$\alpha = \frac{\alpha_\infty}{\alpha^*}\left(\frac{\alpha_o + 0.339 Re_t}{1 + 0.339 Re_t}\right) \tag{13}$$

Note that at the high Reynolds number, $\alpha = \alpha^* = \alpha^*_\infty = \alpha_\infty = 1.0$

$$Y_k = \rho \beta^* f_{\beta^*} k\omega \tag{14}$$

$$f_{\beta^*} = \begin{cases} 1 & \chi_k \le 0 \\ \frac{1 + 680\chi_k^2}{1 + 400\chi_k^2} & \chi_k > 0 \end{cases} \tag{15}$$

$$\chi_k = \frac{1}{\omega^3} \frac{\partial k}{\partial x_j} \frac{\partial \omega}{\partial x_j} \tag{16}$$

$$\beta^* = \beta_i^*[1 + 1.5F(M_t)] \tag{17}$$

$$\beta_i^* = 0.09[0.267 + (0.125Re_t)^4]/[1 + (0.125Re_t)^4] \tag{18}$$

$$Y_\omega = \rho\beta f_\beta \omega^2 \tag{19}$$

$$f_\beta = (1 + 70\chi_\omega)/(1 + 80\chi_\omega) \tag{20}$$

$$\chi_\omega = \left|\frac{\Omega_{ij}\Omega_{jk}S_{ki}}{(0.09\omega)^3}\right| \tag{21}$$

$$\Omega_{ij} = \frac{1}{2}\left(\frac{\partial u_i}{\partial x_j} - \frac{\partial u_j}{\partial x_i}\right) \tag{22}$$

$$\beta = 0.072 - 1.5\beta_i^* F(M_t) \tag{23}$$

Compressibility Correction

The compressibility function $F(M_t)$ is given by,

$$F(M_t) = \begin{cases} 0 & M_t \le M_{to} \\ M_t^2 - M_{to}^2 & M_t > M_{to} \end{cases} \tag{24}$$

$$\mathrm{M}_t^2 = 2k/a^2 \tag{25}$$

$$M_{to} = 0.25 \tag{26}$$

$$a = \sqrt{\gamma RT} \tag{27}$$

Note that at the high Reynolds number, $\beta_i^* = \beta_\infty^*$.

Boundary Conditions

All boundary conditions for wall-function meshes will correspond to the wall-function approach, but in the case of fine meshes the appropriate low Reynolds number boundary conditions will be applied.

$$\text{At the wall } \omega_\omega = \frac{\rho(u^*)^2}{\mu}\omega^+ \tag{28}$$

The asymptotic value of ω^+ in the laminar sublayer is given with respect to the roughness height, k_s, by

$$\omega^+ = \min\left[\omega_\omega^+, 6/\beta_\infty^*(\mathrm{y}^+)^2\right] \tag{29}$$

where

$$\omega_\omega^+ = \begin{cases} \left(\frac{50}{k_s^+}\right) & k_s^+ < 25 \\ \frac{100}{k_s^+} & k_s^+ \ge 25 \end{cases} \tag{30}$$

where

$$\mathrm{k}_s^+ = \max(1.0, \rho k_s u^*/\mu) \tag{31}$$

In the turbulent region, the value of ω^+ is

$$\omega^+ = \frac{1}{\sqrt{\beta_\infty^*}}\frac{du_{\text{turb}}^+}{dy^+} \tag{32}$$

which leads to the value of ω in the wall cell as

$$\omega = \frac{u^*}{\sqrt{\beta_\infty^*}ky} \tag{33}$$

Initial wall temperature, inlet total pressure, and temperature are specified. In the present compressible flow calculations, isentropic relations for an ideal gas are applied to relate total pressure, static pressure, and velocity at a pressure inlet boundary. The specified input of the total pressure, P_t, at the inlet and the static pressure, P_s, in the adjacent fluid cell are thus related as

$$\frac{P_t + P_{\text{op}}}{P_s + P_{\text{op}}} = \left(1 + \frac{(\gamma - 1)v^2}{2\gamma RT_s}\right)^{\gamma/(\gamma-1)} \tag{34}$$

Please note that operating pressure appears in the preceding equation because the given boundary condition inputs are in terms of pressure relative to the operating pressure. The preceding equation was used to compute the velocity magnitude of the fluid at the inlet plane with the given inlet total pressure and total temperature. The static temperature at the inlet, T_s, is computed from the given input of total temperature using the following relation:

$$\frac{T_t}{T_s} = 1 + \frac{\gamma - 1}{2}M^2 \tag{35}$$

Because the DTMs considered here are inert (i.e., no mass addition) at the solid walls a no-slip boundary condition is imposed. At the nozzle exit a pressure profile is imposed. Note that the motor exit geometry (nozzle) considered in this study is a short straight duct followed by the convergent duct. Therefore, it is inevitable to impose a radial axisymmetric pressure distribution at the exit, which is approximated analytically using the well-known equation for radial velocity distribution for duct flows (see Fig. 3). Note that this is more realistic than the conventional assumptions and, moreover, this will not create erroneous solutions. The Courant–Friedrichs–Lewy number is initially chosen as 3.0 in all of the computations. Ideal gas is selected as the working fluid. The transient mass addition due to propellant burning is deliberately suppressed in this model to examine the intrinsic flow features discretely in SRMs with divergent ports.

An algebraic grid-generation technique is employed to discretize the computational domain. A typical grid system in the computational region is selected after the detailed grid refinement

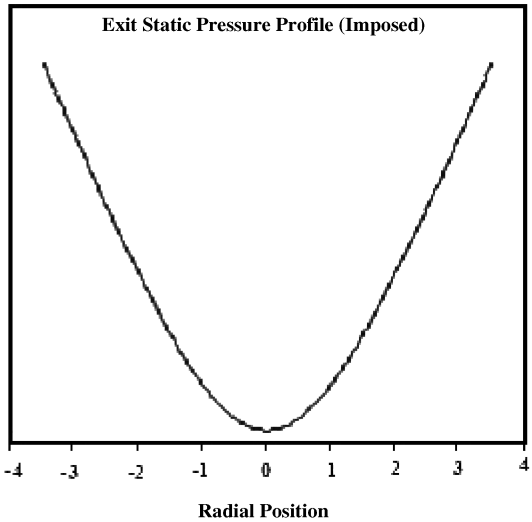

Fig. 3 A typical imposed motor exit pressure profile.

exercises. The grids are clustered near the solid walls using suitable stretching functions. The motor geometric variables and material properties are known a priori. In this study, numerical simulations have been carried out in inert simulators of dual-thrust motors with two different L/d ratios.

Evaluation of Boundary-Layer Blockage

It is assumed that the developing flow can be represented by boundary-layer thickness together with a core in which the velocity is uniform. The approach applies equally to smooth or rough grain surfaces. It is also assumed that the flow consists of two boundary layers of equal thickness. For entry flows of the boundary-layer type, the most important fluid-dynamic parameter that affects the system performance is the area fraction blocked by the boundary-layer displacement thickness. The boundary-layer displacement thickness is widely used in integral methods of boundary-layer theory. In two-dimensional flow, its definition is unambiguous and is given by

$$\delta^* = \int_0^{d/2} \left(1 - \frac{u}{U_{\max}}\right) \mathrm{d}y \tag{36}$$

where y is the distance measured from the port wall, $U_{\max}$ is the velocity on the axis and d is the diameter of the upstream port of the DTM.

The integral continuity equation for unit width is

$$Q = Ud = 2\int_0^{d/2} u \, \mathrm{d}y \tag{37}$$

where U is the mean flow velocity. Combining the preceding two equations results in the blockage

$$\frac{\delta^*}{d/2} = 1 - \frac{U}{U_{\max}} \tag{38}$$

Although many empirical methods are available, an acceptable method of calculating the mean flow velocity, U, is by numerical solution of the flow equations, which is applied here in toto.

It may be mentioned here that, in axisymmetric flow, some researchers continue to use the parameters defined by Eq. (36) and others use revised definitions. Whichever form is used, it is emphasized that considerable care has to be exercised in adapting two-dimensional data to axisymmetric flows.

Results and Discussion

To examine the capability of the code to capture the shock waves, as a first step, the appearance of the igniter induced shock wave was examined in a typical high-velocity transient (HVT) motor with a uniform port but with two different igniter nozzle geometries, viz., convergent and convergent–divergent (CD). The appearance of the shock wave was evident in both the cases [6]. It was noted that the larger the upstream normal Mach number component, the larger the increase in downstream pressure and temperature, and the greater the loss in stagnation pressure, the smaller the downstream Mach number. These features are examined in HVT motors with divergent ports. Note that most of the available models do not capture the shock wave phenomena comprehended by the HVT motors. Nevertheless, one can judge the formation of the shock waves inside the port of any solid rocket motor through an accurate evaluation of the internal fluid flow Mach number. If the igniter shock does not appear in the numerical solution, there is something wrong.

As a second step, the flow features are examined in DTMs with two different upstream port diameters but with the same initial and boundary conditions. An idealized physical model of a typical dual-thrust motor is shown in Fig. 4. Figures 5 and 6 show the grid systems in the computational domain. In both cases, inlet total pressure and total temperature are given as the same input to the code. Igniter geometry is deliberately avoided in this study to examine the intrinsic flow physics pertinent to the *fluid-throat*-induced shock waves in DTMs at subsonic inflow conditions.

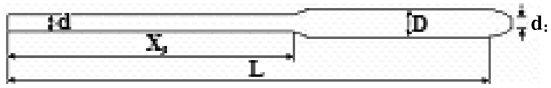

Fig. 4 Idealized physical model of a typical dual-thrust motor.

Fig. 5 Grid system in the computational region of a dual-thrust motor with a narrow-upstream port (case 1: $L/d = 44.4$, $d_t/D = 0.58$, $L/D = 17.85$).

Fig. 6 Grid system in the computational region of a dual-thrust motor with a wide-upstream port (case 2: $L/d = 28.6$, $d_t/D = 0.58$, $L/D = 17.85$).

In case 1 (see Fig. 5), attention is focused on a dual-thrust motor with a narrow-upstream port and with steep divergence. The port geometry ($d_t/D = 0.58$, $L/D = 17.85$, $L/d = 44.4$) is selected based on a typical DTM. The initial total pressure and temperature are specified as input to the code (i.e., at $t = 0+$, $P_i = 209,000$ Pa, $T_i = 690$ K, $k = 196$ m^2/s^2, and $\omega = 44,494$ s^{-1}) and a pressure profile is imposed at the exit. Except for the geometric variables, all other parameters are kept constant in the parametric studies. Figure 7 demonstrates the axial velocity variation of the DTM at different time intervals. It is evident from this figure that the velocity magnitude is high at the transition location ($x/X_s = 1$). This can be explained with the help of boundary-layer theory. Note that, owing to the viscous friction, a boundary layer will be formed on the walls (before the transition region) and their thickness will increase in the downstream direction to the divergence location. Because the volume of flow must be the same for every section, the decrease in the rate of flow near the walls that is due to friction must be compensated for by a corresponding increase near the axis. Thus, the boundary-layer growth occurs under the influence of an accelerated external flow. As a result, at larger distances from the inlet section velocity will be relatively high and the flow will possibly become turbulent; consequently, the boundary-layer thickness will suddenly increase leading to the sudden increase in the axial velocity due to the rocket motor port area fraction being blocked by the boundary-layer displacement thickness. This will cause flow separation far downstream of the divergence region, which will alter the reattachment/secondary ignition point. The sudden increase in axial velocity is evident in Fig. 7.

Note that the thickness of a turbulent boundary layer is larger than that of a laminar boundary layer owing to greater energy loss in the former. The development of the wall boundary layer in turbulent flow is more complicated than in wholly laminar flow. Initially it takes the form of a laminar layer, but at some position along the rocket motor port there is a transition to a turbulent layer, where a sudden increase in axial velocity can be discerned (see Fig. 7). At time $t = 0.1$ ms, a sudden increase in the centerline axial velocity is discerned at $x/X_s = 0.84$. When time advances the location of the sudden increase in axial velocity was shifted toward the head end of the motor, presumably because of the flow transition from laminar to turbulent (see Fig. 7, $t = 0.1$–0.3 ms). The actual position of transition in a real motor depends on a number of factors including Reynolds number, surface roughness, and the turbulence level of the igniter jet flow entering the motor port. Figure 8 shows the corresponding Mach number variations of the DTM. It is evident that, at the given subsonic inflow conditions and without any igniter nozzle or geometrical throat inside the port of the motor, the flow gets accelerated to a higher Mach number ($M > 1$) near the transition region, at $t = 10$ ms, and suddenly dropped to a lower Mach number ($M < 1$). It is presumed that the flow must have accelerated through a throat, which is sonic. The way in which the flow adjusts itself to maintain sonic velocity at the throat depends on the conditions downstream of the throat. Figures 9–12 clearly show that the entire

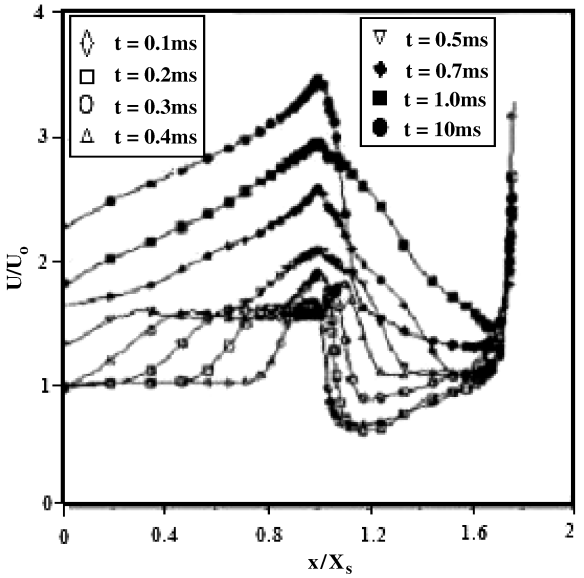

Fig. 7 Velocity variations along the axis of the DTM at different time intervals showing that the peak velocity is near the transition region ($L/d = 44.4$).

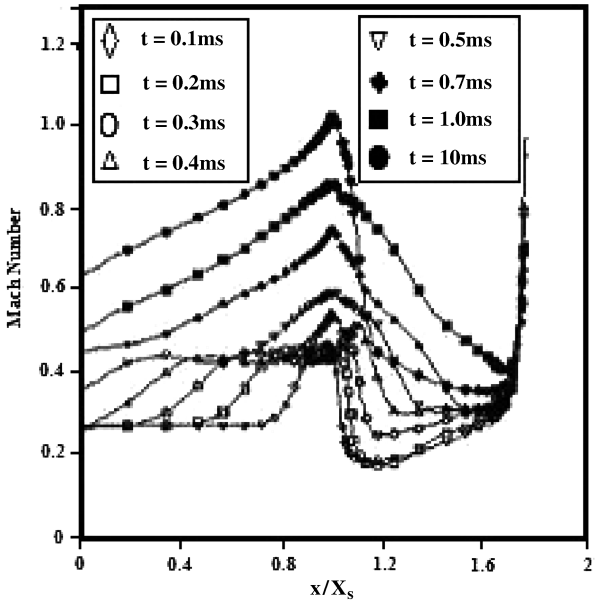

Fig. 8 The axial variation of the Mach number along the axis of the DTM at different time intervals showing that the flow gets accelerated to a higher Mach number ($M > 1$) at the transition location ($x/X_s = 1$) at subsonic inflow conditions (corresponding to Fig. 7).

flow is subsonic inside the DTM except at the transition region. It has been noticed that the DTM nozzle remains unchoked. It may be recalled here that, owing to the viscous friction, a boundary layer could be formed on the walls of the HVT motors (before the transition region), and their thickness will increase in the downstream direction to the divergent location leading to the formation of a temporary *fluid throat* at the transition location due to the area fraction being blocked by the boundary-layer displacement thickness. As a result, in general, at larger distances from the inlet section (X_s) velocity will be high at the transition location and this will lead to the formation of shock waves in HVT motors with a narrow port combined with a steep divergence. This obviously will contribute to the high-pressure spike in real motors during the starting transient.

In Fig. 13 the ratio of the axial velocity, $U_{\max}$, to the mean flow velocity, U, at the narrow-upstream port of the motor is shown as a function of axial distance with reference to the divergence location,

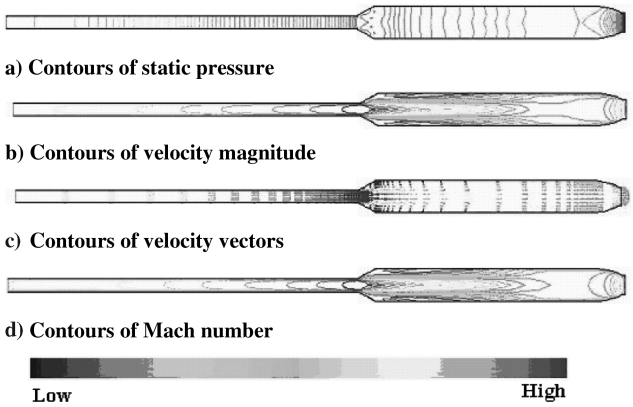

Fig. 9 Demonstrating the flowfield of a dual-thrust motor ($L/d = 44.4$) before choking ($t = 0.7$ ms).

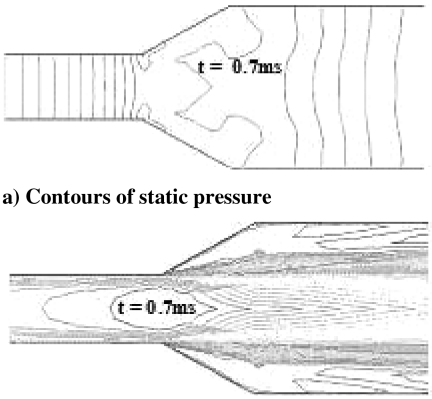

Fig. 10 Enlarged view of the contours at the transition region of a DTM before choking (corresponding to Fig. 9).

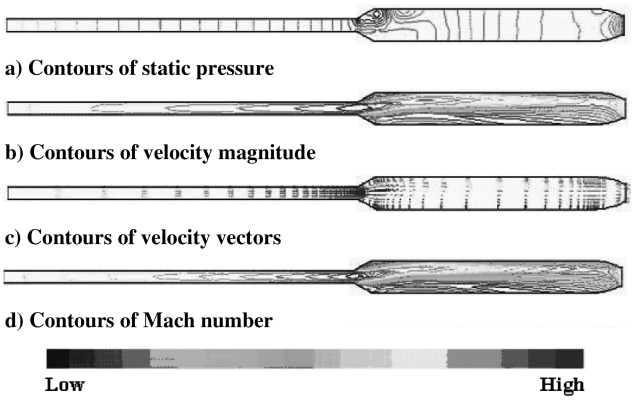

Fig. 11 Demonstrating the flowfield of a dual-thrust motor ($L/d = 44.4$) after choking ($t = 10$ ms).

X_s. As anticipated, a slight velocity oscillation is observed during a short period of time (i.e., up to $t = 0.3$ ms), and this has been reflected in the subsequent figures too. Figure 14 shows the corresponding variations of the blockage at the narrow-upstream port of the DTM, evaluated from the displacement thickness, up to the transition region ($x/X_s = 1$) at different time intervals. A sudden increase in blockage is evident at different axial locations during the flow transition period. This figure is corroborative evidence of the area blockage at the transition region, which amounts to the internal flow choking at the transition region of the DTM. Around 30% area blockage is observed at the transition region at $t = 1$–10 ms. This is sufficient to propose the temporary formation of a *fluid–solid CD nozzle* at the transition region. As a result, the upstream narrow port of the DTM will act like a second igniter to the downstream

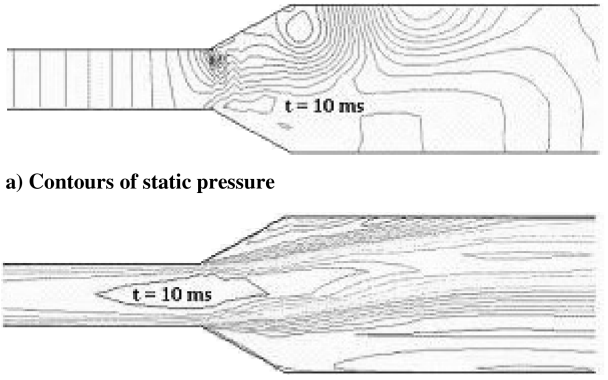

a) Contours of static pressure

b) Contours of Mach number

Fig. 12 Enlarged view of the contours at the transition region of a DTM after choking (corresponding to Fig. 11).

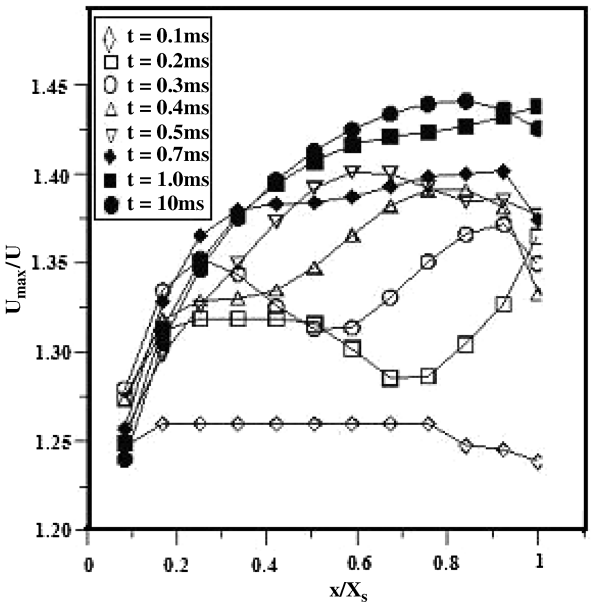

Fig. 13 Demonstrating the variations of the mean velocity in the developing flow with reference to the axial velocity.

port leading to the formation of possible shock waves inside the DTM.

Normal shock waves, which we normally assume to be simple discontinuities in the flow, occurring at a discrete cross section in practice have more complicated geometries, in part simply due to the nonuniformity of the velocity profile, but also due to the complex interaction of the shock wave with the viscous flow in the vicinity of the duct walls. Note that large adverse pressure gradients are imposed on a moving stream by the presence of a shock. The slow moving fluid close to the wall of the duct has insufficient momentum to negotiate this pressure gradient. As a consequence, depending upon the original thickness of the boundary layer and strength of the shock wave, thickness of the boundary layer or even flow separation occurs near the wall, and in the central portion of the flow a complex oblique shock pattern may be established. The presence of a shock implies that the flow is choked.

The experience gained through the full motor static tests and flight motor data revealed that increasing the upstream port area of the dual-thrust motor could negate the undesirable pressure spike [2,10,11]. In an attempt to understand the intrinsic flow physics to that effect and in light of the new findings, different parametric analytical studies have been carried out. In case 2, it has been observed that when the upstream port area of the DTM was increased by 55% (i.e., L/d ratio reduced to 28.6) the formation of the *sonic fluid throat* was not discerned with the same initial and boundary

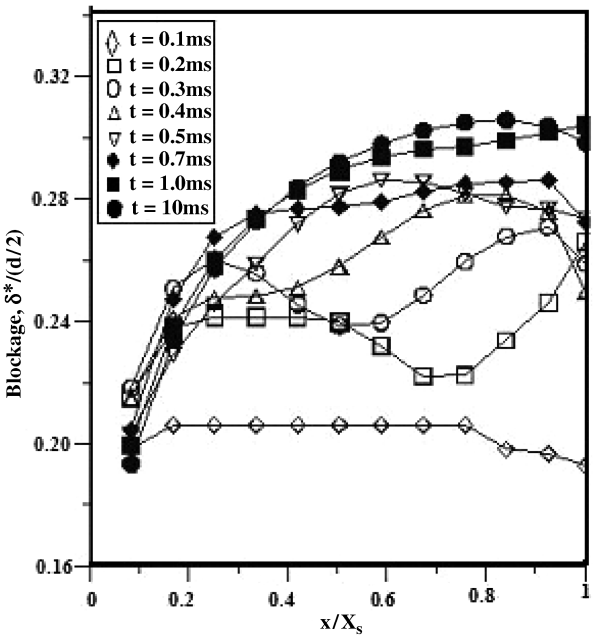

Fig. 14 Demonstrating the variations of the blockage factor in the upstream port of a DTM ($L/d = 44.4$) during the flow development.

conditions. This was done without altering the other geometric variables ($d_t/D = 0.58$, $L/D = 17.85$) of the DTM. When compared with case 1, a substantial reduction in blockage factor is noticed in case 2. Figure 15 shows the comparison of the blockage at the different upstream axial locations of the DTMs. This was estimated based on Eq. (38). It is presumed that the maximum in this figure is associated with the coalescence of the boundary layer on the axis of the motor port. These are corroborated with the available experimental findings [17,18]. Figures 16 and 17 show the axial (centerline) velocity and the corresponding Mach number variations, at different time intervals, of the aforesaid DTMs. It has been observed that after the flow gets choked at the nozzle throat ($t = 1.5$ ms), the velocity at the transition region has marginally decreased and there was no evidence of choking condition at the transition location and the maximum Mach number observed within the motor was only 0.48. This reveals that, with the same inflow conditions but with relatively large upstream port area, the flow will not accelerate to a higher Mach number ($M > 1$) leading to the

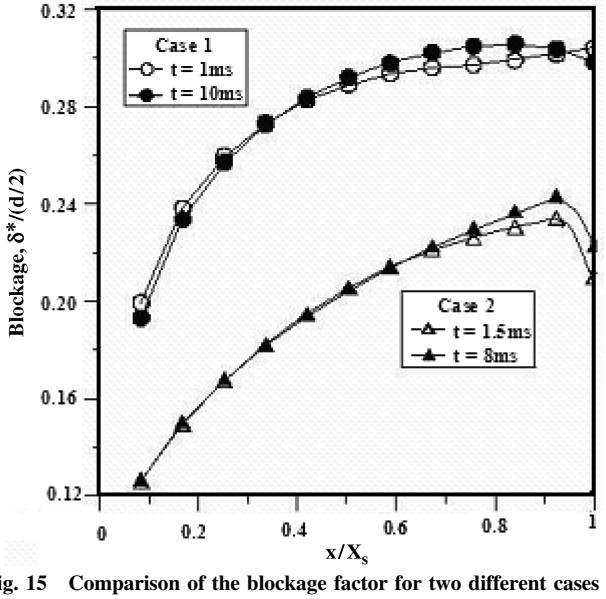

Fig. 15 Comparison of the blockage factor for two different cases of DTM with two different L/d ratios (case 1: $L/d = 44.4$; case 2: $L/d = 28.6$).

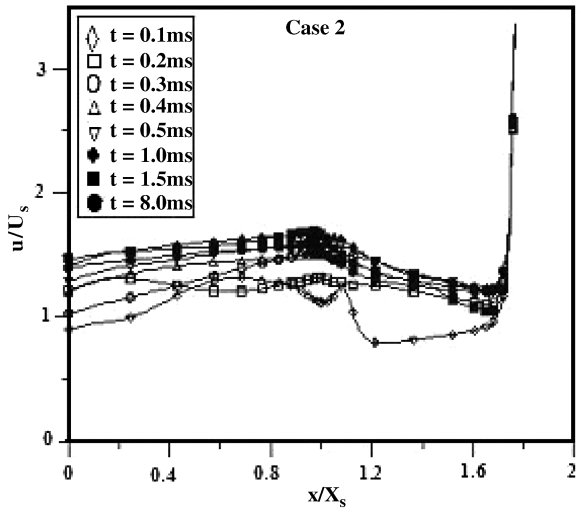

Fig. 16 Velocity variations along the axis of the DTM with an enlarged upstream port at different time intervals ($L/d = 28.6$).

formation of shock waves inside the rocket motor. Note that shock waves, boundary-layer thickness, and turbulence are familiar concepts, yet they are not easy to define in such a way as to cover the detailed flow characteristics encountered in the HVT motors. Nevertheless, the results from the full-scale static tests of the DTM (see Fig. 1) and flight data (for instance, see Fig. 2) of high-performance rockets with different upstream port areas qualitatively supported these theoretical discoveries [10,11].

Analysis further revealed that there is no evidence of thermal choking or choking due to high igniter mass flow rate, on the DTM case on hand. These are corroborative evidences of the formation of a shock wave in the transition region due to a different physical origin named the *fluid-throat* effect. The shock wave pattern is merely the mechanism the flow adopts to adjust the pressure distribution between the sonic point and the condition on the flow downstream.

Note that near a solid surface flow velocities are low due to the no-slip condition at the wall. Hence, in a region where the piezometric pressure is increasing, there are likely to exist certain streamlines on which there are points whose total pressure is less than the piezometric pressure a little further downstream. When this happens, these streamlines can only reach this further point if their energy is increased by the action of the shear force exerted by adjacent elements of the flow. This condition is satisfied when $\partial\tau/\partial y > 0$, where τ is the local shear stress and y is the distance measured away from the grain wall. This process of energy conversion by the action of viscosity cannot be maintained indefinitely and, if the flow does not manage to negotiate the region of adverse pressure gradient, a point is reached at which the value of τ and hence of $\partial u/\partial y$ becomes zero at the surface. Downstream of such a point, which is known as a separation point, the velocity u close to the surface becomes negative and so a region of reverse flow is established (see Figs. 9 and 11). Because of their ability to transfer momentum laterally, turbulent flows are more able than laminar flows to negotiate regions of adverse pressure gradients. Whether or not separation actually takes place, the general effect of the adverse pressure gradient is to give rise to a localized region of slow moving fluid stretching away from the wall. Because of the continuity condition, which can be applied over the whole cross-sectional area, the axial flow velocities must necessarily increase elsewhere to compensate for this effect. There is therefore a tendency for flows to become increasingly nonuniform whenever positive axial pressure gradients are encountered (see pressure contours in Figs. 9–12). Figures 11b and 11c show that, after choking, the velocity is no longer symmetrical about the centerline (compare to Figs. 9b and 9c before choking). It is possible that the internal flow oscillates and at 10 ms the flow just happens to be deflected upwards instead of downwards due to the formation of shock waves. This dynamic of the internal flow deserves special attention in the fluid-dynamics community.

Note that in both cases in the head-end region of the DTM a boundary layer grows from the port wall and the core of the motor port is filled by fluid that has nearly uniform velocity. Note that the turbulent boundary layer grows to fill the entire cross section and the core disappears. Following the elimination of the core, further changes in the velocity profile, and in the turbulent structure, continue to occur within the flow. At the stage when the core is just eliminated, the velocity distribution is such that there is a well-defined peak velocity on the motor axis before the transition region, and appreciable variations in velocity occur over the whole cross section. As the flow further develops the peak in the velocity profile gradually disappears until a much flatter distribution is established in the center of the motor port, the largest changes in velocity being confined to a narrow region near the port walls. Eventually, the fully developed state is attained (see Figs. 18–20).

Figure 18 shows the comparison of the inlet ($x/X_s = 0$) velocity profiles of case 1 and case 2 at different time intervals up to the time of convergence ($t = t_{eq}$). Figures 19a–19f and 20a–20f show the dissection of the velocity up to X_s at six different axial locations of

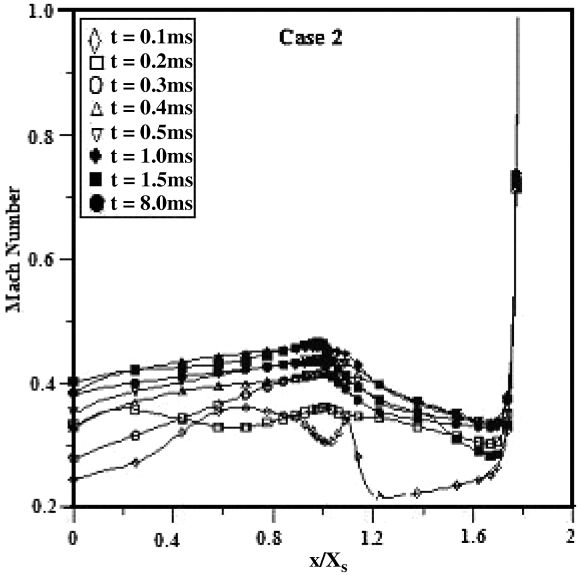

Fig. 17 Demonstrating the axial variation of the Mach number along the axis of the DTM with an enlarged upstream port (corresponding to Fig. 16).

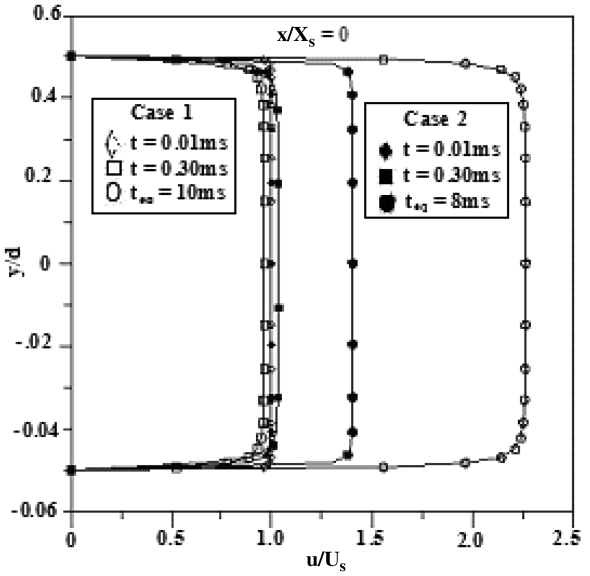

Fig. 18 Comparison of the inlet ($x/X_s = 0$) velocity profiles of case 1 and case 2 at different time intervals up to the time of convergence ($t = t_{eq}$).

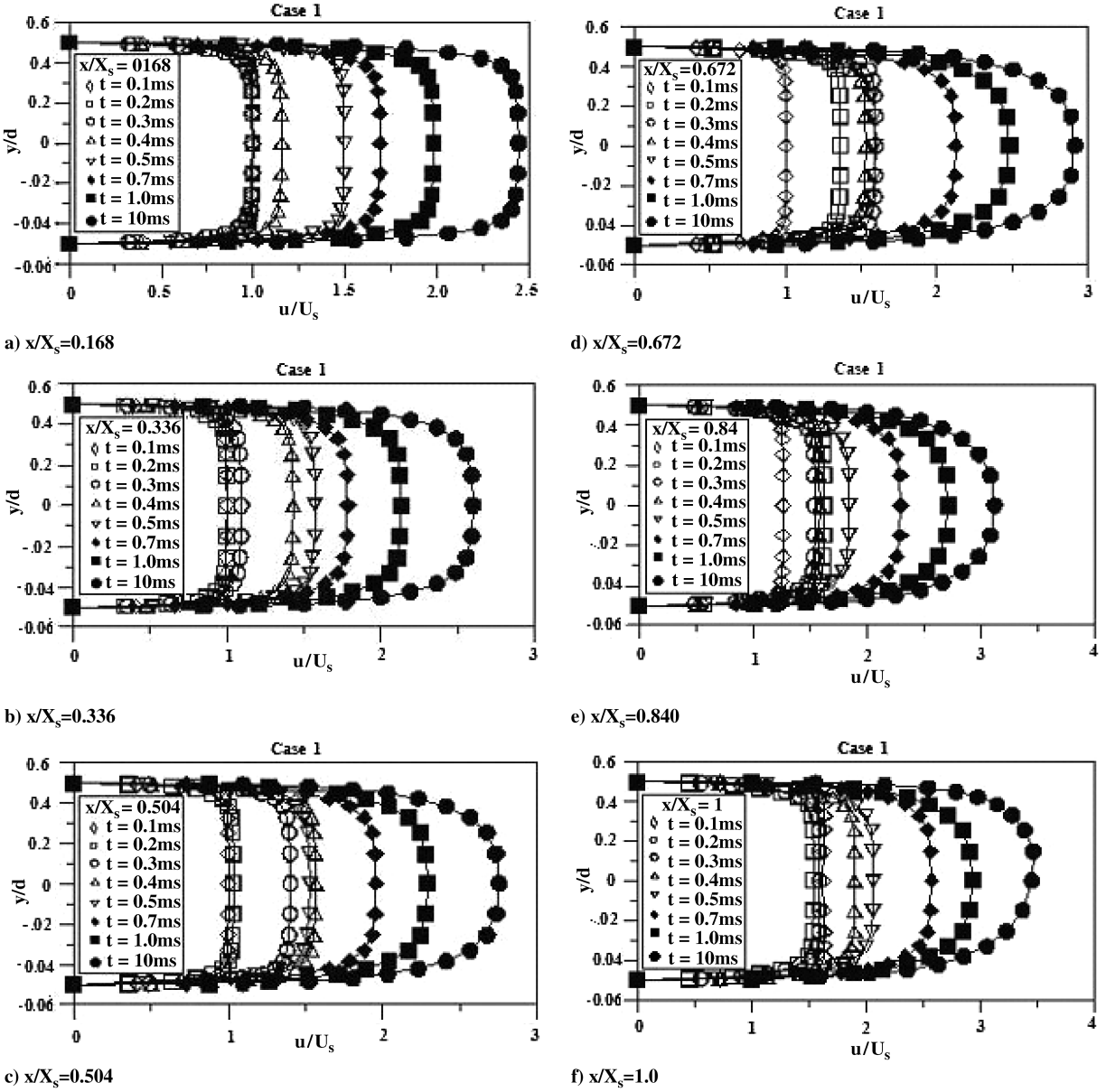

Fig. 19 Velocity history at the upstream port of a DTM (case 1: $L/d = 44.4$) during the internal flow choking.

the DTMs at different time intervals to facilitate the comparison of the sequence of the flow transition at the upstream region of case 1 and case 2. Figure 19f shows the deviation of the maximum velocity from the DTM axis at $t = 10$ ms. Evidently this is because of the flow distortion due to the shock wave. The authors have conjectured that the shock waves in DTMs can generate additional turbulence. The fact is that the reference velocity will be less after shocks, which could increase the turbulence intensity. Note that the turbulence intensity is the ratio of the magnitude of the root mean square turbulent fluctuations of the jet to the reference velocity. The reference value specified should be the mean velocity magnitude for the flow. It was also observed that a case with a narrow-upstream port shows high mean velocity.

Numerical computations were continued until the solutions converged. In case 2 (see Fig. 16), the solution was converged at $t = 8$ ms. Note that by that time the flow is choked at the nozzle end and not at the transition location. At the transition location ($x/X_s = 1$) the Mach number observed was 0.48. But in case 1, the solution was converged at $t = 10$ ms and choked flow condition was observed at the transition location (see Fig. 7 at $x/X_s = 1$) before the nozzle choking. Note that these time scales can be altered by altering the igniter gas temperature. In real motors, the time scale of ignition pressure spike depends on many factors including the igniter jet characteristics, ignition delay, propellant properties, and motor geometry. It was observed through static tests that ignition delay (45–200 ms), time at motor peak (100–500 ms), and time at igniter peak (20–50 ms) altered at identical test conditions too. It was reported previously through different parametric analytical studies that altered variations of igniter characteristics, propellant properties, grain surface effects, ignition delay, and motor configuration effects could alter the time scale of the igniter/motor peak pressure [9]. In a nutshell, with reference to the present computational fluid dynamics results, it may be noted that the small time scale (10 ms) adopted in this analysis will not dilute the proposed postulation on internal flow choking due to the *fluid-throat* effect.

The apparently obvious inference that can be drawn from this study is that the possibility of the occurrence of a choked flow condition at the transition region of the DTM with a narrow-upstream port is very high. This will lead to the formation of shock waves inside the rocket motor. It has been observed that when the upstream port area was large, the formation of the *sonic fluid throat* was not discerned with the same igniter jet flow. Note that when the upstream port area of the DTM was narrow, the ignition pressure spike observed during the full-scale static test was in the order of five times that of the steady-state value. But this pressure spike was not observed during the full-scale static tests of DTMs with the enlarged

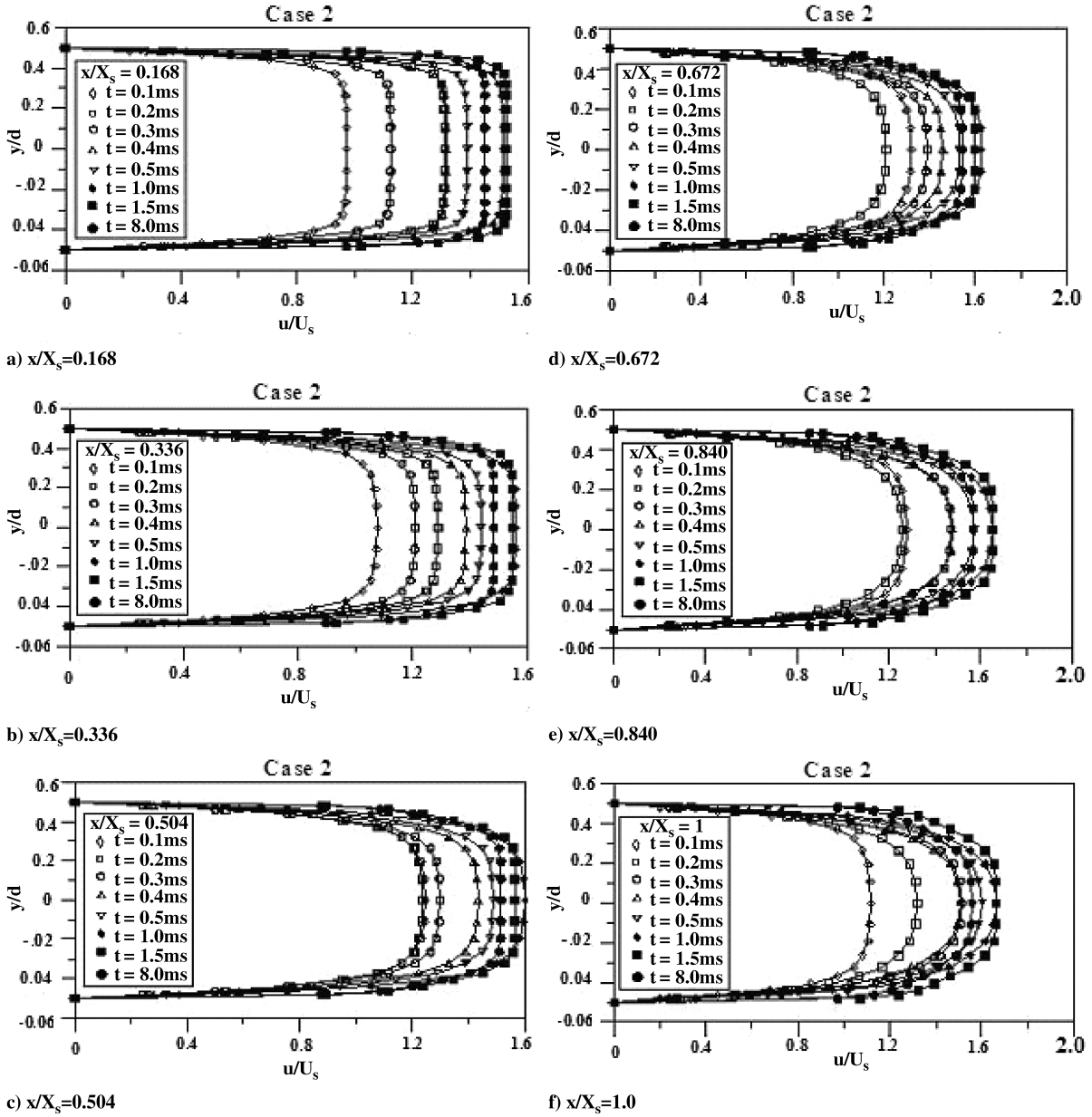

Fig. 20 Velocity history at the upstream port of a DTM (case 2: $L/d = 28.6$), a case without choking.

upstream port area and with the same igniter. This technique was also successfully applied to a certain class of flight motors of Indian origin for reducing the magnitude of the ignition pressure spike. As stated in the connected Note [3], this remedy (i.e., enlarging the upstream port area) has affected the high-performance nature of the rocket motor.

In another attempt with a different HVT motor, the influence of igniter jet turbulence intensity on flow separation has been examined. The separated flow characteristics such as size of the separation bubble, flow redevelopment, and heat transfer in the recirculation region are dependent on the upstream flow features and the grain geometry. A case with high-turbulence intensity shows less possibility of flow separation and reattachment. Therefore, by inducing a high-turbulence level (practically by using igniter nozzle wire screens or by creating artificial roughness to the grain wall without affecting the ballistics), the position of transition could be brought closer to the entry region or, indeed, the laminar layer could be entirely eliminated. Separation is mostly an undesirable phenomenon because it entails large energy losses. In the real motor test cases, the exact location of the secondary ignition point will possibly be altered from the reattachment point due to the additional influence of the igniter ballistics, ignition delay, propellant combustion, etc. Therefore, for pinpointing the exact location of the secondary ignition one has to consider the intrinsic fluid dynamics and combustion aspects of the rocket motor and its allied igniter [2,5]. Note that the location of the reattachment point and/or secondary ignition and the features of the recirculation bubbles are sensitive to the port geometry and the igniter jet turbulence intensity. The implication of the secondary ignition can be quite serious for DTMs [5]. Applying inhibitors at the exact secondary ignition location can prohibit multiple flame fronts formation and ballisticians can thereby attenuate the possible ignition peak and pressure-rise rate due to that effect without sacrificing the propellant loading density of DTMs. This can be verified through the full motor static test.

In the process of identifying which phenomenon or combination of phenomena was causing the pressure spike, pressure-rise rate, and pressure oscillations in HVT motors with divergent port, the importance of hitherto unexpected flow features of dual-thrust motors have come to the foreground. Through these findings, ballisticians can explore possible remedies (like boundary-layer trips) for eliminating the unacceptable pressure spikes and pressure oscillations often experienced due to internal flow choking in dual-thrust motors without diluting their high performance.

Conclusions

The difficulties associated with solving compressible flows are a result of the high degree of coupling between the flow velocity, density, pressure, and energy. This coupling may lead to instabilities in the solution process and, therefore, one may require special solution techniques to obtain a converged solution. In addition, the presence of shocks in the flow introduces an additional stability problem in the calculation. Through the present theoretical study we concluded that, in addition to the igniter induced shock waves, there is a possibility of the occurrence of shock waves in dual-thrust motors with a narrow-upstream port and with steep divergence, due to the formation of a *fluid throat* at the beginning of the transition region due to the area fraction being blocked by boundary-layer displacement thickness. As a result, the upstream narrow port will act like a second igniter to the downstream port of the motor leading to possible shock waves inside the rocket motor. Downstream of the shock, the flow experiences an adverse pressure gradient, usually leading to wall boundary-layer separation and reattachment. The seemingly obvious conclusion that can be drawn from this study is that the possibility of the occurrence of a choked flow condition at the transition region of the DTM with a narrow-upstream port is very high and that might lead to the formation of shock waves. In the real motor, this phenomena will lead to the formation of a high-pressure spike often in the order of five times that of the steady-state pressure values (see Fig. 1). When the upstream port area was increased by 55% the blockage factor was found decreased by 25%. Certainly this reduction in blockage factor will negate/delay the choking at the transition region and will supplement the DTM for an early nozzle choking. The fact is that if the height of the upstream port relative to the motor length is too small, the developing boundary layers from either side of the port can interact, leading to a choked flow. On the other hand, if the developing boundary layers are far enough apart, then choking does not occur. It was observed that the blockage factor is greater in magnitude for the choked case than for the unchoked case. It may be noted here that most of the available models do not capture the shock wave phenomena encountered in the DTMs. Nevertheless, the accurate evaluation of the Mach number along the axis is sufficient to propose the possible occurrence of shock waves in DTMs. Shock waves, both normal and oblique, are events that occur over a very short distance, typically the same order of magnitude as the mean free path, that is, 10^{-7} m. From the point of view of continuum theory, they can be treated as localized discontinuities within the flow, which everywhere else satisfies the continuum hypothesis. The authors have conjectured that the shock waves in DTMs can generate additional turbulence. The shock waves and the new turbulence level will alter the location of the reattachment/secondary ignition point and also enhance the heat flux to the propellant surface, which in turn will enhance the flame spread rate and the transient burning. As a result, the effective flame spread time required for the complete propellant surface area to be ignited decreases drastically, giving rise to a high-pressure-rise rate in the second phase of the starting/ignition transient. This effect will be further accentuated in the case of a star grain downstream of a sudden expansion (see the inset of Fig. 1), where the star points generate multiple flame fronts. The cumulative effects of this entire phenomenon would result in the amplification of the pressure spike, the pressure-rise rate, and the thrust oscillations during the mission of dual-thrust motors, which is beyond the scope of this paper. This paper is a pointer toward meeting high-performance rocket motor design challenges without altering the mission demanding thrust-time trace shape requirements.

Acknowledgments

V. R. Sanal Kumar would like to thank the Korea Science and Engineering Foundation (KOSEF) and the Indian National Science Academy (INSA), New Delhi for providing all possible support for the completion of this work through the overseas research program. V. R. Sanal Kumar would also like to thank all the editors and the reviewers of the Journal of Fluid Mechanics, Journal of Spacecraft and Rockets, and Journal of Propulsion and Power for their constructive suggestions for the completion of this work. Acknowledgment is also extended to all coresearchers for their judicious help and support in unveiling this theory. The authors would also like to acknowledge the contributions of A. Sameen, Visiting Researcher.

References

[1] Peretz, A., Kuo, K. K., Caveny, L. H., and Summerfield, M., "Starting Transient of Solid Propellant Rocket Motors with High Internal Gas Velocities," *AIAA Journal*, Vol. 11, No. 12, 1973, pp. 1719–1729.

[2] Sanal Kumar, V. R., Raghunandan, B. N., Kim, H. D., Sameen, A., Setoguchi, T., and Raghunathan, S., "Starting Transient Flow Phenomena in Inert Simulators of SRMs with Divergent Ports," *Journal of Propulsion and Power*, Vol. 22, No. 5, Sept.–Oct.–Feb. 2006, pp. 1138–1141. doi:10.2514/1.16439

[3] Sanal Kumar, V. R., Raghunandan, B. N., Kim, H. D., Sameen, A., Setoguchi, T., and Raghunathan, S., "Studies on Internal Flow Choking in Dual-Thrust Motors," *Journal of Spacecraft and Rockets*, Vol. 43, No. 5, Sept.–Oct. 2006, pp. 1140–1143. doi:10.2514/1.20748

[4] Sanal Kumar, V. R., Kim, H. D., Raghunandan, B. N., Sameen, A., Setoguchi, T., and Raghunathan, S., "Fluid-Throat Induced Shock Waves During the Ignition Transient of Solid Rockets," *Journal of Spacecraft and Rockets*, Vol. 43, No. 1, Jan.–Feb. 2006, pp. 225–228.

[5] Raghunandan, B. N., Sanal Kumar, V. R., Unnikrishnan, C., and Sanjeev, C., "Flame Spread with Sudden Expansions of Ports of Solid Rockets," *Journal of Propulsion and Power*, Vol. 17, No. 1, 2001, pp. 73–78.

[6] Sanal Kumar, V. R., Kim, H. D., Raghunandan, B. N., Setoguchi, T., Mastuo, S., and Raghunathan, S., "Studies on Shock Waves in Solid Rocket Motors," *International Symposium on Shock Waves*, Vol. 1, Indian Institute of Science, Bangalore, India, 17–22 July 2005.

[7] Raghunandan, B. N., Madhavan, N. S., Sanjeev, C., and Sanal Kumar, V. R., "Studies on Flame Spread with Sudden Expansions of Ports of Solid Propellant Rockets Under Elevated Pressure," *Defence Science Journal*, Vol. 46, No. 5, Nov. 1996, pp. 417–423.

[8] Sanal Kumar, V. R., Kim, H. D., Raghunandan, B. N., Setoguchi, T., and Raghunathan, S., "Internal Flow Simulation of High-Performance Solid Rockets Using a k–ω Turbulence Model," *Journal of Thermal Science, International Journal of Thermal and Fluid Sciences*, Vol. 14, No. 2, June 2005, pp. 114–119. doi:10.1007/s11630-005-0020-4

[9] Sanal Kumar, V. R., "Flame Spread and Starting Transient in Solid Rocket Motors with Non-Uniform Port," Ph.D. Dissertation, Dept. of Aerospace Engineering, Indian Institute of Science, Bangalore, India, Oct. 2001.

[10] Raghunandan, B. N., "Diagnostic Investigation of Ignition Problems in High-Performance Rocket Motors," Indian Institute of Science, ISRO Space Technology Cell, AE Dept., Rept. ISTC/AE/BNR/043, Bangalore, India, 1995.

[11] Sanal Kumar, V. R., "A Ballistic Explanation of Ignition Peak of PSLV Third Stage Motor," Vikram Sarabhai Space Center, Technical Rept. PHC/VRS/PS-TR-93, Trivandrum, Kerala, India, Dec. 1993.

[12] Ikawa, H., and Laspesa, F. S., "Ignition/Duct Overpressure Induced by Space Shuttle Solid Rocket Motor Ignition," *Journal of Spacecraft and Rockets*, Vol. 22, No. 4, July–Aug. 1985, p. 481.

[13] Salita, M., "Modern SRM Ignition Transient Modeling (Part 1): Introduction and Physical Models," AIAA Paper 2001-3443, 2001.

[14] Alestra, S., Terrasse, I., and Troclet, B., "Identification of Acoustic Sources at Launch Vehicle Lift-Off Using an Inverse Method," AIAA Paper 2002-926, 2002.

[15] Kumar, M., and Kuo, K. K., "Flame Spreading and Overall Ignition Transient," *Fundamentals of Solid Propellant Combustion*, edited by K. K. Kuo and M. Summerfield, Vol. 90, Progress in Astronautics and Aeronautics, AIAA, New York, 1984, pp. 305–360.

[16] Sanal Kumar, V. R., "Thermoviscoelastic Characterization of a Composite Solid Propellant Using Tubular Test," *Journal of Propulsion and Power*, Vol. 19, No. 3, 2003, pp. 397–404.

[17] Krall, K. M., and Sparrow, E. M., "Turbulent Heat Transfer in the Separated, Reattached, and Redevelopment Regions of a Circular Tube," *Journal of Heat Transfer*, Vol. 88, No. 2, Series C, 1966, pp. 131–136.

[18] Stevens, S. J., and Fry, P., "Measurements of the Boundary-Layer Growth in Annular Diffusers," *Journal of Aircraft*, Vol. 10, No. 2, Feb. 1973, pp. 73–80.

[19] Sabnis, J. S., Gibeling, H. J., and McDonald, H., "Navier–Stokes

Analysis of Solid Propellant Rocket Motor Internal Flows," *Journal of Propulsion and Power*, Vol. 5, No. 6, Nov.–Dec. 1989, pp. 657–664.
[20] Eagar, M. A., Luke, G. D., and Stockham, L. W., "Ignition Transient Modelling for the Space Shuttle Advanced Solid Rocket Motor," AIAA Paper 1993-2062, 1993.
[21] Blomshield, F. S., and Mathes, H. B., "Pressure Oscillations in Post-Challenger Space Shuttle Redesigned Solid Rocket Motors," *Journal of Propulsion and Power*, Vol. 9, No. 2, March–April 1993, pp. 217–221.
[22] Clayton, J. L., "Modeling of the Space Shuttle Solid Rocket Motor Nozzle Boot Cavity Pressurization Process," *Journal of Spacecraft and Rockets*, Vol. 26, No. 5, Sept.–Oct. 1989, pp. 385–390.
[23] Purcell, S. P., Daines, W. L., and Christensen, L. W., "Simulation of the Pressure Gradient in a Segmented Solid Rocket Motor During the Ignition Transient," AIAA Paper 1992-3822, 1992.
[24] Foster, W. A., Sforzini, R. H., and Shackelford, B. W., "Thrust Imbalance of the Space Shuttle Solid Rocket Motors," *Journal of Spacecraft and Rockets*, Vol. 19, No. 6, Nov.–Dec. 1982, pp. 545–549.
[25] Johnston, W. A., "Solid Rocket Motor Internal Flow During Ignition," *Journal of Propulsion and Power*, Vol. 11, No. 3, 1995, pp. 489–496.
[26] Caveny, L. H., Kuo, K. K., and Shackelfold, B. W., "Thrust and Ignition Transients of the Space Shuttle Solid Rocket Motor," *Journal of Spacecraft and Rockets*, Vol. 17, No. 6, Nov. –Dec. 1980, pp. 489–494.
[27] Fiedler, R. A., Haselbacher, A., Breitenfeld, M. S., Alexander, P., Masaa, L., and Ross, W. C., "3-D Simulation of Ignition Transient in the RSRM," AIAA Paper 2005-3993, 10–13 July 2005.
[28] Sforzini, R. H., and Fellows, H. L., "Prediction of Ignition Transients in Solid-Propellant Rocket Motors," *Journal of Spacecraft and Rockets*, Vol. 7, No. 5, 1970, pp. 626–628.
[29] Chao, Y.-C., Chou, W.-F. and Liu, S.-S., "Computation of Turbulent Reacting Flow in a Solid-Propellant Ducted Rocket," *Journal of Propulsion and Power*, Vol. 11, No. 3, 1995, pp. 473–482.
[30] Balachandar, S., Buckmaster, J. D., and Short, M., "The Generation of Axial Vorticity in Solid-Propellant Rocket-Motor Flows," *Journal of Fluid Mechanics*, Vol. 429, No. 1, Feb. 2001, pp. 283–305. doi:10.1017/S0022112000002688
[31] Luke, G. D., Eager, M. A., and Dwyer, H. A., "Ignition Transient Model for Large Aspect Ratio Solid Rocket Motors," AIAA Paper 96-3273, 1996.
[32] Fabignon, Y., Dupays, J., Avalon. G., Vuillot, F., Lupoglazoff, N., Casalis, G., and Prevost, M., "Instabilities and Pressure Oscillations in Solid Rocket Motors," *Aerospace Science and Technology*, Vol. 7, No. 3, April 2003, pp. 191–200. doi:10.1016/S1270-9638(02)01194-X
[33] Manson, D. R., Folkman, S. K., and Behring, M. A., "Thrust Oscillations of the Space Shuttle Solid Rocket Booster Motor During Static Tests," AIAA Paper 79-1138, 1979.
[34] Johnston, W. A., "A Numerical Procedure for the Analysis of the Internal Flow in a Solid Rocket Motor During the Ignition Transient Period," AIAA Paper 91-1655, 1991.
[35] Lupoglazoff, N., Vuillot, F., Dupays, J., and Fabignon, Y., "Numerical Simulation of the Unsteady Flow Inside Ariane 5 P230 SRM Booster with Burning Aluminium Particle," *Second European Conference on Launcher Technology*, European Space Agency, Paris, Nov. 2000.
[36] Apte, S., and Yang, V., "An LES Study of Transition and Flow Instability in a Porous-Walled Chamber with Mass Injection," *Journal of Fluid Mechanics*, Vol. 477, March 2003, pp. 215–225. doi:10.1017/S0022112002002987
[37] Wilcox, D. C., *Turbulence Modeling for CFD*, DCW Industries, Inc., La Canada, CA, 1998.

J. Oefelein
Associate Editor